Journal of Power Sources 467 (2020) 228230

Contents lists available at ScienceDirect

Journal of Power Sources

journal homepage: www.elsevier.com/locate/jpowsour

Ceramic synthesis of disordered lithium rich oxyfluoride materials

Jean-Marcel Ateba Mba [a], Iztok Arčon [b,c], Gregor Mali [a], Elena Tchernychova [a], Ralf Witte [d], Robert Kruk [d], Miran Gaberšček [a,e], Robert Dominko [a,e,f,*]

[a] National Institute of Chemistry, Hajdrihova 19, 1000, Ljubljana, Slovenia
[b] University of Nova Gorica, Vipavska 13, 5000, Nova Gorica, Slovenia
[c] Institute Jožef Stefan, Jamova 39, 1000, Ljubljana, Slovenia
[d] Institute of Nanotechnology, Karlsruhe Institute of Technology, 76344, Eggenstein-Leopoldshafen, Germany
[e] FKKT, University of Ljubljana, Večna pot 117, 1000, Ljubljana, Slovenia
[f] ALISTORE-ERI, FR3104, 80039, Amiens Cedex, France

HIGHLIGHTS

- Lithium rich iron/titanium oxyfluoride materials synthesized by ceramic synthesis route.
- Low level of doping leads to regions rich in transition metal and the area rich in Li.
- Level of doping has an impact on electrochemical activity.
- The highest capacity was obtained with samples having low level doping.

ARTICLE INFO

Keywords:
Lithium batteries
Face centered-cubic
Oxyfluoride
Li-rich
Disorder

ABSTRACT

Disordered lithium-rich transition metal oxyfluorides with a general formula $Li_{1+x}MO_2F_x$ (M being a transition metal) are gaining more attention due to their high specific capacity which can be delivered from the face-centered cubic (*fcc*) structure. The most common synthesis procedure involves use of mechanosynthesis. In this work, ceramic synthesis of lithium rich iron oxyfluoride and lithium rich titanium oxyfluoride are reported. Two ceramic synthesis routes are developed each leading to the different level of doping with Li and F and different levels of cationic disorder in the structure. Three different $Li_{1+x}MO_2F_x$ samples ($x = 0.25$, 0.3 and 1) are compared with a sample prepared by mechanochemical synthesis and non-doped $LiFeO_2$ with fcc structure. The obtained lithium rich iron oxyfluoride are characterized by use of Mössbauer spectroscopy, X-ray absorption spectroscopy, NMR and TEM. Successful incorporation of Li and F have been confirmed and specific capacity that can be obtained from the samples is in the correlation with the level of disorder introduced with doping, nevertheless oxidation state of iron in all samples is very similar. Conclusions obtained from lithium rich iron oxyfluoride are validated by lithium rich titanium oxyfluoride.

1. Introduction

High energy-density cathode materials are the main focus in the search for new compounds that can be used as an active materials for Li-ion batteries. Among all proposed families of cathode materials, a lithium transition metal oxides are the most studied due to their versatility in composition and structure. The structures of these materials can be layered, spinel or face centered-cubic (*fcc*). The latter are based on the sodium chloride structure with the oxygen atoms in the close packed *fcc* sites and the cations filling all the octahedral interstices. A family of lithium transition metal oxides ($LiMO_2$ with M being a transition metal) is an example of *fcc* materials. $LiMO_2$ were obtained by ball-milling (mechanosynthesis) [1] and exhibited a poor electrochemical behaviour. It has been shown that lithium-rich material (Li_xMO_2 with $x > 1$) can overcome that issue [2]. The good performances observed in lithium-rich oxide composition are due to the formation of a percolating network of low-energy migration pathways that do not require lithium ions to pass directly adjacent to a transition metal [2]. Moreover, compared to $LiMO_2$, where maximum 1 Li^+ can be extracted per formula unit, Li-rich Li_xMO_2 offers a possibility to extract more than 1 Li^+ from

* Corresponding author. National Institute of Chemistry, Hajdrihova 19, 1000, Ljubljana, Slovenia.
E-mail address: robert.dominko@ki.si (R. Dominko).

https://doi.org/10.1016/j.jpowsour.2020.228230
Received 29 January 2020; Received in revised form 15 April 2020; Accepted 20 April 2020
Available online 26 May 2020

the structure leading to improved capacity.

The charge balance at a lithium-rich composition can be done by the substitution of the oxygen anion by fluorine. This has been well demonstrated by oxyfluoride materials such as Li_2VO_2F [3,4], Li_2CrO_2F [5] and Li_2MnO_2F [6] obtained by mechanosynthesis. Indeed, the mechanical stress generated during the synthesis is forcing LiF to get incorporated in the $LiMO_2$ host structure and a certain degree of cationic disorder is introduced into the structure [7]. The mechanosynthesis leads to the formation of the meta-stable phase in a highly non-equilibrium state with the compositional inhomogeneity [3,6]. Moreover, the creation of the partially amorphous phase as well as poor reactants intermixing at the atomic scale has been reported [8,9].

Family of Li_2MO_2F obtained by mechanosynthesis (M = V, Cr or Mn) crystalizes in *fcc* structure. As proposed [3], Li and M occupies randomly the same *4a* crystal sublattice (with an occupancy factor of ~66 at.% for Li and ~33 at.% for M). Similarly O^{2-} and F^- occupies randomly the Wyckoff position *4b* in the same structure (with occupancy ratio of ~66 at.% and ~33 at.% for O and F respectively). Therefore, the structure can be described as a layered phase, in which Li/M cations and O/F segregate into layers in the cubic (111) direction.

As proposed by computational chemistry, improved crystallinity and better distribution of atoms can be obtained by ceramic synthesis [2]. The authors constructed a phase diagram of $LiFeO_2$–LiF from DFT-derived cluster expansions, and showed the possibility to synthesize Li_2FeO_2F phase at temperature above 1200 °C. To the best of our knowledge, an experimental procedure for the ceramic synthesis of Li_2MO_2F has never been reported.

In this study, we demonstrate the possibility to synthesize $Li_{1+x}FeO_2F_x$ (with $0 < x < 1$) and $Li_{1+x}TiO_2F_x$ (with $0 < x < 1$) samples with *fcc* rock-salt structure by ceramic synthesis based on two different precursors. The major advantage of iron and titanium based materials is their abundances and environmental acceptance. Additionally, iron samples can be characterized by different techniques. The structural, compositional and electrochemical properties of $Li_{1+x}FeO_2F_x$ are compared with sample prepared by mechanochemical synthesis and with a sample prepared without LiF doping (*i.e.* $LiFeO_2$). Important structural and compositional properties are derived by combined analysis using X-ray diffraction, Mössbauer spectroscopy, X-ray absorption spectroscopy, ^{7}Li and ^{19}F solid state NMR and HR-TEM microscopy. The study of the ceramic synthesis was further extended to titanium oxyfluoride $Li_{1+x}TiO_2F_x$. In both cases, the observed properties were directly related to the electrochemical characteristics of samples investigated in this study. Finally, observed correlations between the cationic disorder and electrochemical activity of lithium iron oxyfluoride were confirmed by set of samples based on titanium transition metal.

2. Experimental section

Synthesis: For mechanosynthesis (ms), stoichiometric amounts of Fe_2O_3 (respectively Ti_2O_3) (both from Alfa Aesar Puratronic), Li_2O (from Alfa Aesar) and LiF (from Aldrich) (total mass of *ca.* 5 g) were introduced into zirconium oxide jar together with 25 balls of 10 mm of diameter. A planetary grinder from Retsch (RETSCH PM 200) was used at a speed rate of 600 rpm (with a reverse rotation every hour) during 48 h. For the Fe based material, the color of the recovered material was brownish and it was labelled as LFF-ms. The Ti based material displayed a grayish color and was labelled LTF-ms.

For the first ceramic synthesis route (cs1), three different stoichiometric amounts of Fe_2O_3, Li_2O and LiF (1:1:y, where y = 2, 0.6 and 0.5) were thoroughly mixed in the mortar, pressed as pellets and sealed into a stainless steel reactor (Figure SI 1) inside the glovebox to ensure that the pellet was in an inert atmosphere during the synthesis. The reactor was introduced into a furnace, which was heated at 850 °C for 3 h followed by quenching in liquid nitrogen. The recovered black pellets were crushed in a mortar. Three different compositions were labelled related to the amount of LiF as precursor: LFF-cs1-100, LFF-cs1-30 and LFF-cs1-25 respectively. In the second ceramic synthesis route (cs2), we used different precursors, FeF_3 and Li_2O, while preparation of the sample and calcination procedure was similar as in the first approach. However, due to hydrophilic nature of FeF_3 all preparation was done in the argon atmosphere. The recovered grey powder was labelled LFF-cs2. For sake of comparison, pure phase of $LiFeO_2$ was synthesized using stoichiometric amount of Fe_2O_3 and Li_2O. The same process as described above was applied and the recovered black powder was labelled LFO.

We applied synthesis approaches cs1 and cs2 to the titanium analogous. For both approaches we used Ti_2O_3 and TiF_3 as precursors, respectively. The optimum temperature was 900 °C and optimum time was found to be 20 min.

X-Rays diffraction: Powder X-ray diffraction was performed on PANalytical, configured with Ge(111) monochromator (Johansson type) giving Cu Kα1 in Bragg-Brentano reflection geometry. The range used was 10°–120° in 2θ at a step size of 0.008° (time per step 550 s). The lattice parameters were refined using Edpcr software in Fullprof_suite program.

Neutron powder diffraction was performed at the high-intensity neutron powder diffractometer, Wombat, at ANSTO (λ = 1.539(2) Å) over a 120° 2θ range (16°–136°).

X-Absorption Spectroscopy: Fe K-edge XAS and spectra of lithium iron oxide and oxyfluoride cathode materials with *fcc* rock-salt structure (LFF-ms, LFF-cs1-25, LFF-cs2, LFO) were measured at XAFS beamline of Elettra synchrotron radiation facilities in transmission detection mode. A Si (111) double crystal monochromator was used with 0.8 eV energy resolution at 7 keV. Higher-order harmonics were effectively eliminated by detuning the monochromator crystals to 70% of the rocking curve maximum. The intensity of the monochromatic X-ray beam was measured by three consecutive 30 cm long ionization detectors respectively filled with the following gas mixtures: 580 mbar N_2 and 1420 mbar He; 90 mbar Ar, 1000 mbar N_2 and 910 mbar He; 350 mbar Ar, 1000 mbar N_2 and 650 mbar He. The absorption spectra were measured within the interval [-200 eV–1100 eV] relative to the Fe K edge. In the XANES energy region equidistant energy steps of 0.2 eV were used, while for the EXAFS region equidistant k steps of 0.03 Å-1 were adopted with an integration time of 1 s/step. The duration of one XAS scan was 30 min.

The battery samples with lithium iron oxide and oxyfluoride cathode materials were prepared in a pouch cell used for operando studies of Li-ion batteries [10]. The reference Fe compounds samples (Fe_2O_3, Fe_3O_4, $FeSO_4$) were prepared in the form of homogenous pellets, pressed from micronized powder mixed with boronitrate (BN). In all cases the total absorption thickness of the sample was about 2 above the Fe K-edge.

Sample pellets were placed between the first and second ionization cell. The exact energy calibration was established with simultaneous absorption measurement on a 5-μm thick Fe metal foil placed between the second and the third ionization chamber. Absolute energy reproducibility was ±0.02 eV.

The analysis of XANES and EXAFS spectra is performed with Demeter (IFEFFIT) program package [11], in combination with FEFF6 program code [12] for ab initio calculation of photoelectron scattering paths.

NMR: Solid-state ^{7}Li and ^{19}F magic-angle spinning (MAS) NMR spectra were recorded on a 600 MHz Varian NMR system, operating at ^{7}Li Larmor frequency of 232.97 MHz and ^{19}F Larmor frequency of 564.06 MHz. Varian 1.6 mm HXY MAS probehead at sample rotation frequency of 40 kHz was used. ^{7}Li MAS NMR spectrum of each sample was obtained as a sum of a series of spin-echo sub-spectra recorded at different irradiation frequencies [13]. The irradiation-frequency step was 80 kHz (*i.e.* twice the sample rotation frequency). Each sub-spectrum was phase corrected to zero order. Durations of the first and the second pulse in the rotation-synchronized spin-echo experiment were 1.4 and 2.8 μs, respectively, and the delay between the pulses was 25 μs (i.e. one rotation period). Repetition delay between consecutive scans was 10 s, and number of scans for each individual spectrum was 32. The frequency axes of the ^{7}Li MAS NMR spectra were reported

relative to the signal of Li_2SiO_3 (0 ppm). ^{19}F MAS NMR spectrum of each sample was also obtained as a sum of a series of spin-echo sub-spectra recorded with the irradiation-frequency step of 80 kHz. Durations of the first and the second pulse in the ^{19}F MAS spin-echo experiment were 1.25 and 2.5 μs, respectively, and the delay between the pulses was 25 μs. Repetition delay between consecutive scans was 0.25 s, and number of scans for each individual spectrum was 1280. Because of the short repetition delay, narrow (slowly relaxing) contributions to the ^{19}F NMR spectra were somewhat suppressed with respect to the broad (quickly relaxing) contributions. For all the ^{19}F NMR spectra strong, broad background signal (stemming from the stator) had to be subtracted. The frequency axes of the ^{19}F MAS NMR spectra were referenced using a signal of NaF at −221 ppm.

^{57}Fe MÖSSBAUER SPECTROSCOPY: ^{57}Fe Mössbauer spectra were collected using a standard transmission Mössbauer setup with a ^{57}Co in Rh-Matrix source operated in constant acceleration mode. All spectra are measured at room temperature with a maximum velocity scale of 3.5 mm/s, which was calibrated with a metallic Fe foil. All Isomer shifts (IS) are given with respect to metallic, bcc-Fe at room temperature. The spectra are fitted using the WinNormos for Igor software.

TEM: Samples were hand grind in a mortar prior to be dispersed in ethanol. Few drops of the mixed solution were deposit on the lacey carbon covered TEM copper grid. The morphology, composition and the atomic structure of the synthesized materials were assessed by means of transmission electron microscopy. For these analyses, a probe aberration-corrected JEM-ARM200CF equipped with JEOL Centurio 100 mm2 EDXS detector, JEOL STEM detectors (JEOL, Tokyo, Japan) and Gatan GIFQuantum (Gatan, Plesanton, USA) EELS spectrometer, was employed. Fe, O and F elemental distribution was assessed by electron energy-loss spectroscopy in STEM mode (STEM-EELS).

ELECTROCHEMISTRY: The electrochemical tests were performed in Swagelok cell assembled in an argon-filled dry glove box. Prior to be used, the active materials were ball milled with 15 wt % of C_{65} carbon black (from TIMCAL) and 10 wt % of PVdF-HFP during 30 min at 300 rpm. In order to ensure porosity and rapid electrolyte uptake within the electrodes, 33 wt % of Dibutylphtalate (DBP) was added [14]. Finally, some drops of NMP were added for appropriate viscosity, and the slurry was stirred for 2 h prior to be casted on a glass plate using a doctor blade (with a gap of 500 μm). After drying, electrodes of 12 mm in diameter were cut and pressed together with Al-mesh disk. The obtained electrodes were soaked in diethyl ether in order to remove DBP. The electrodes loading were between 3 and 4 mg/cm^2. The cells consisted of the positive electrode (as described above), Li disk as negative electrode, and 1 M of $LiPF_6$ in a mixture of EC-DEC (1:1) as electrolyte (LP40). The assembled cells were cycled between 3 V and 1.3 V vs. Li^+/Li. Electrochemical impedance spectra were recorded in VMP3 potentiostat/galvanostat in the frequency range of 1 MHz–1 μm Hz. Electrochemical half-cell was discharged for 2 h at C/20 then relaxed for 4 h. The EIS spectra were recorded at the end of each relaxation. The GITT measurements consisted of series of current-pulses applied at a rate of C/50 during 1 h, followed by a long relaxation time for which the condition was set to dV/dT < 4 mV/h.

3. Results and discussion

As controlled experiment, we prepared first lithium iron oxyfluoride by mechanosynthesis (LFF-ms) and the LeBail refinement of the lattice parameters of the XRD pattern is presented in the Fig. 1. As stated in the experimental part, LFF-ms was obtained by mixing stoichiometric quantities of iron oxide (Fe_2O_3), lithium oxide (Li_2O) and lithium fluoride (LiF). The pathway for the formation of the phase is proposed in the Equation (1).

$$Fe_2O_3 + Li_2O + 2LiF \rightarrow 2Li_2FeO_2F \quad (1)$$

LFF-ms crystallizes in a single phase that can be well refined with *fcc*

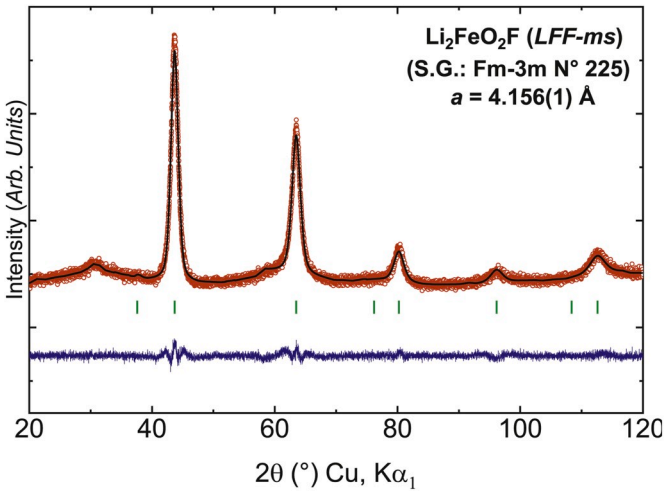

Fig. 1. Observed (red dots), calculated (black line), and difference (blue line) plots obtained for the fullpattern matching refinement of X-ray diffraction data for Li_2FeO_2F obtained by ball-milling and labelled LFF-ms. (For interpretation of the references to color in this figure legend, the reader is referred to the Web version of this article.)

structure (S.G. N° 225), with the lattice parameter of 4.156(1) Å. The first ceramic synthesis route proceeded through the Equation (1). XRD pattern (Figure SI2) of the sample (LFF-cs1-100) indicates the presence of two phases in the final product; both crystalized in *fcc*. The simulated XRD pattern (Figure SI2), which is a sum of the contributions of the $LiFeO_2$ and LiF phases, is very close to the measured pattern. However, one can notice that the diffraction peaks of $LiFeO_2$ are shifted to higher 2θ values in the simulated XRD pattern, suggesting that the lattice parameter (a = 4.177(7) Å) of LFF-cs1-100 is higher compared to the lattice parameter of the usual $LiFeO_2$ (a = 4.162 Å ICSD N° 44879). The shift of diffraction peaks toward lower 2θ values is indication of at least partial incorporation of LiF into the *fcc* structure. Namely, the XRD pattern containing diffraction peaks of LiF (ICSD N° 51208) suggests that not all of the LiF was consumed in the reaction. In order to decrease the residual LiF, the stoichiometric ratio of LiF compare to Fe_2O_3 was gradually reduced.

By systematic work we decreased quantity of LiF by using reaction mixture with the molar ratio of 1:1:0.60 (for Fe_2O_3, Li_2O and LiF) (Figure SI3), whereas the molar ratio of 1:1:0.50 showed only minor LiF impurities in the sample (Fig. 2a). Therefore, we can conclude that the final product of the latter synthesis setup has a composition close to $Li_{1.25}FeO_2F_{0.25}$ (labelled LFF-cs1-25). Here, the composition is derived with the precision of the XRD technique. Equation (2) is a chemical equation, which describes the pathway for the successful formation of LFF-cs1-25:

$$Fe_2O_3 + Li_2O + 0.5LiF \rightarrow 2Li_{1.25}FeO_2F_{0.25} \quad (2)$$

Note, that Equation (2) can be split in two parts as

$$Fe_2O_3 + Li_2O \rightarrow 2LiFeO_2 \quad (2a)$$

$$LiFeO_2 + 0.25LiF \rightarrow Li_{1.25}FeO_2F_{0.25} \quad (2b)$$

However, the split pathway where the synthesis of $LiFeO_2$ compound was followed by the subsequent incorporation of LiF was proven unsuccessful. This is in line with the DFT calculation [2] which demonstrated poor solubility of LiF phase in $LiFeO_2$ phase at temperatures below 1200 °C. As stated in the experimental part, synthesis was performed in the inert atmosphere since synthesis in air leads to the formation of Fe_3O_4 phase. Moreover the syntheses performed without a rapid quench in N_2 liquid lead to the formation of $LiFeO_2$ and LiF phases. Quenching was therefore performed in order to avoid phase

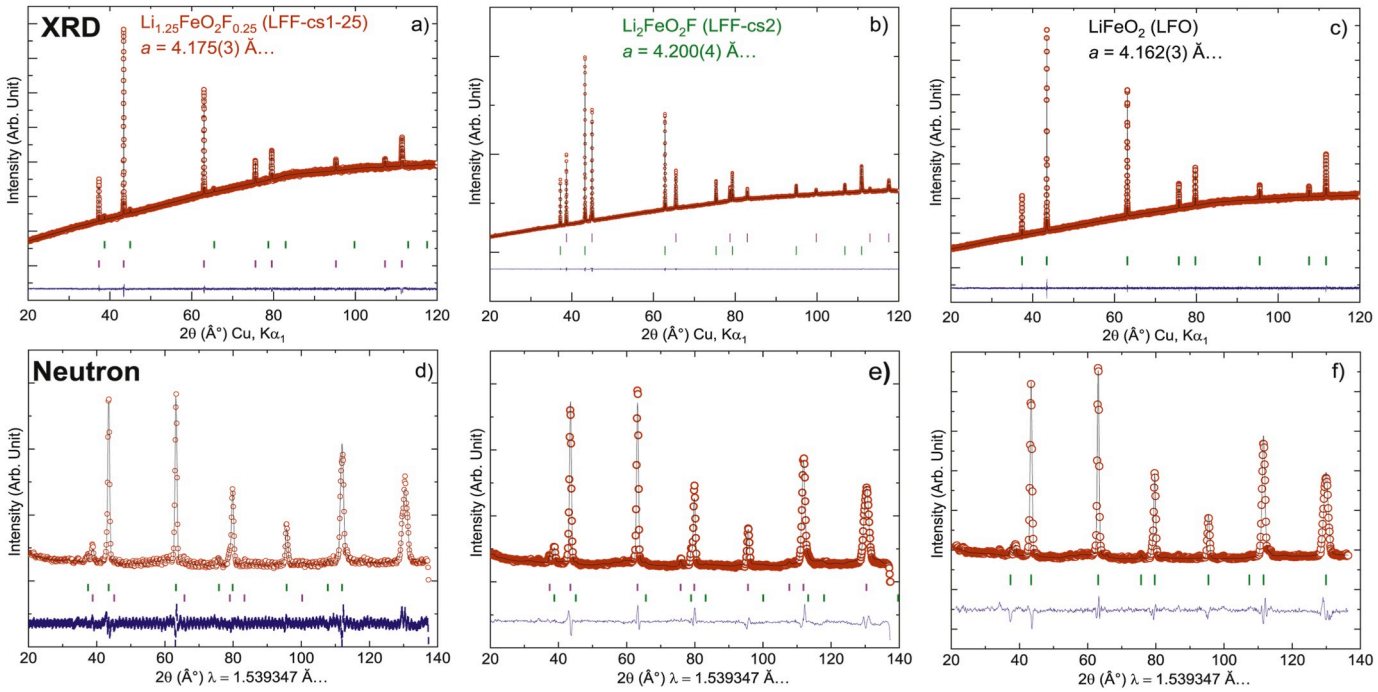

Fig. 2. Full pattern matching refinement (using Le Bail method) of X-ray diffraction patterns for different samples prepared in this work, when amount of: (a) LFF-cs1-25; (b) LFF-cs2; (c) LFO, and refined Neutron diffraction patterns with composition derived from refinement for (d) LFF-cs1-25; (e) LFF-cs2; (f) LFO samples.

dismutation.

The first ceramic synthesis route (cs1) could only deliver the LFF-cs1-25 composition with the Li excess of 0.25 and fully incorporated F amount of 0.25 (e.g. $Li_{1.25}FeO_2F_{0.25}$). In order to have a higher Li enrichment, we developed a different ceramic synthesis route (cs2). Here, a stoichiometric mixture of FeF_3 and Li_2O was reacted in order to form a phase pure, fully doped Li_2FeO_2F (sample LFF-cs2). The XRD pattern and the lattice parameter are recorded in Fig. 2b. The reaction of those precursors in stoichiometric proportion leads to the formation of LiF according to the Equation (3). Moreover, Gibbs energy of formation of LiF is highly negative ($\Delta_f G^{LiF} = -607$ kJ/mol) and LiF is the main phase formed within above described mixture. Therefore, Li_2FeO_2F phase can be considered a by-product, as shown in the Equation (3).

$$FeF_3 + 2Li_2O \rightarrow Li_2FeO_2F + 2LiF \quad (3)$$

$$FeF_3 + 2Li_2O \rightarrow LiFeO_2 + 3LiF \quad (4)$$

Note, that in the Equation (3) and (2) moles of LiF are formed in order to have Li_2FeO_2F. The Equation (4) demonstrates the possibility of forming 3 mol of LiF. In that case $LiFeO_2$ is formed as a by-product. The excess of LiF formed according to both Equations (3) and (4) can be washed out with cold water (temperature close to freezing point). The materials are stable upon washing since no structural changes have been observed by XRD (no change in the lattice parameters see figure SI4). Moreover, the fact that washing is very effective can be seen in the Figure SI 5, which compares ^{7}Li MAS NMR spectra of LFF-cs2 before and after washing.

In order to confirm formation of the product from the Equation (3), we have synthesized pure $LiFeO_2$ phase by using stoichiometric amount of Fe_2O_3 and Li_2O. The XRD results revealed that the lattice parameter of the phase obtained by LFF-cs2 (Fig. 2b) is higher than that of synthesized LFO (Fig. 2c). For all the investigated ceramic synthesis materials, the lattice parameter "*a*" increases with the increase of fluorine content.

Crystal structure and composition of LFF-cs1-25, LFF-cs2 and LFO samples were additionally checked by Neutron diffraction, which enables quantification of lithium in the crystalline material. The refinement of both XRD and Neutron diffraction reached a satisfactory reliability factor (see Fig. 2 d-f and Table SI1-SI4). The occupancy factor obtained for each phase indicate that the stoichiometry is according to Equations (2) and (3).

Mössbauer spectroscopy was employed to detect differences in the chemical environment and oxidation state of Fe influenced by LiF incorporation into the structure. Spectra of all investigated samples displayed a quadrupolar splitting of the absorption lines, and spectral fitting for all samples was done assuming four quadrupole doublets (see Fig. 3 and Table 1). The main component of all spectra was characteristic of Fe^{3+}. In order to represent this component adequately and in agreement with literature, data were represented by using two doublets with similar isomer shift (IS) and different quadrupole splitting (QS). The values of IS were characteristic of high spin trivalent iron ions in octahedral sites in both cases; however the larger QS of sub-spectrum B indicated a larger electric field gradient at the nucleus site.

This spectral feature was observed for the first time for the $LiFeO_2$ phase by D.E. Cox et al. [15] and explained by O. Knop et al. [16] According to Knop, the random distribution of cations Li^+ and Fe^{3+} on the corner and the face-centered positions in the cubic lattice around the Fe^{3+} nuclei create different electric field gradients due to the difference in charge of the neighbouring ions due to partial short-range ordering.

According to that, doublet A in Fig. 3 with smaller QS is attributed to ^{57}Fe sites with mostly Li^+ as nearest neighbours, in agreement with investigations on the chemically ordered isostructural compound $NaFeO_2$ [17]. Doublet B, in its turn, is assigned to sites with a distribution of Li^+ and Fe^{3+} neighbours. Note, that the attempts to fit the data with only one broadened doublet result in systematic features in the difference spectrum.

Besides the majority Fe^{3+} component, also a minor Fe^{2+} component was visible in the shoulder at positive velocities of the main doublet. As the XRD investigation does not evidence any additional phase, the observation of a Fe^{2+} component can be explained by the presence of oxygen vacancies in the investigated materials. This is a reasonable assumption as it has been shown that reducing fully oxidized $LiFeO_2$ with CaH_2[18] results in very similar spectra.

Moreover, both cs1 and cs2 routes presented here include a high temperature treatment in a sealed reactor (high pressure) and in an inert

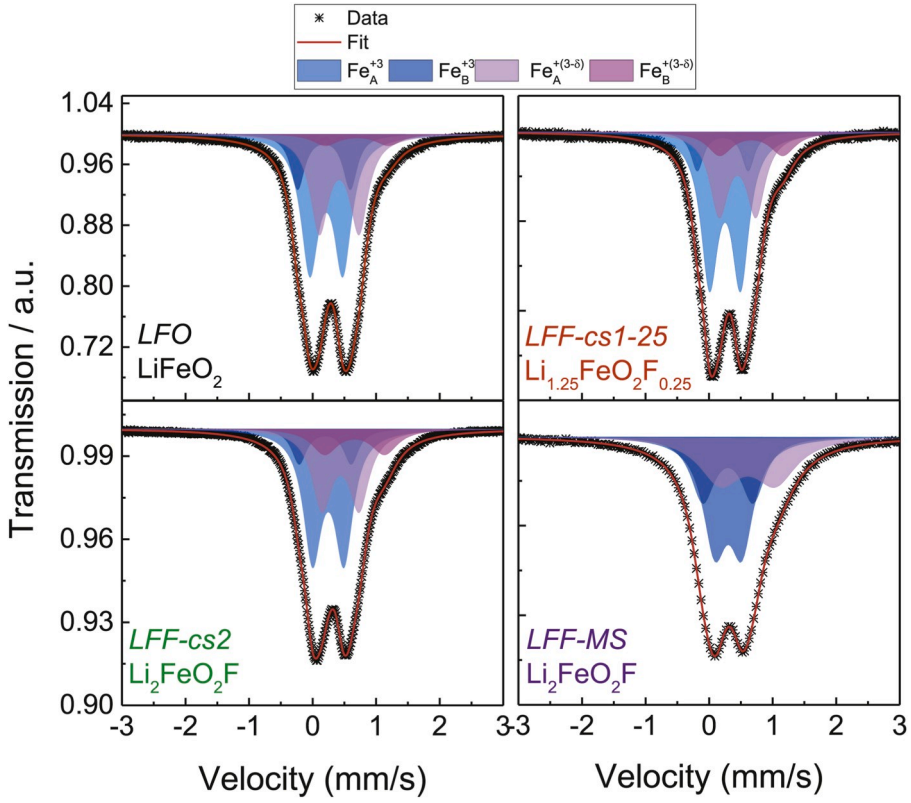

Fig. 3. Room temperature 57Fe Mössbauer spectra of as-prepared materials.

Table 1
Mössbauer data table.

Sample	SS	IS (mm/s)	QS (mm/s)	Gamma (mm/s)	Area	2.3
LFO $LiFeO_2$	A	0.320 (2)	0.52(1)	0.34(1)	45	Fe^{3+}
	B	0.286 (2)	0.83(1)	0.27(1)	15	
	C	0.525 (2)	0.62(1)	0.35(1)	34	$Fe^{(3-\delta)+}$
	D	0.704 (2)	1.00(1)	0.48(1)	6	
LFF-cs1-25 $Li_{1.25}FeO_2F_{0.25}$	A	0.362 (1)	0.49(1)	0.33(1)	50	Fe^{3+}
	B	0.323 (1)	0.8(1)	0.25(1)	10	
	C	0.562 (1)	0.58(1)	0.36(1)	29	$Fe^{(3-\delta)+}$
	D	0.773 (1)	1.00(1)	0.48(1)	11	
LFF-cs2 Li_2FeO_2F	A	0.352 (2)	0.50(2)	0.35(1)	46	Fe^{3+}
	B	0.304 (5)	0.82(2)	0.29(1)	10	
	C	0.548 (5)	0.58(1)	0.39(2)	31	$Fe^{(3-\delta)+}$
	D	0.770 (7)	0.95(2)	0.50(3)	13	
LFF-ms Li_2FeO_2F	A	0.39(3)	0.43(2)	0.45(2)	42	Fe^{3+}
	B	0.40(1)	0.79(2)	0.46(2)	26	
	C/D	0.72(1)	0.87(1)	0.80(2)	32	$Fe^{(3-\delta)+}$

atmosphere (argon), which may lead to a partial reduction. Following the above argument, for the fitting of the Fe^{2+} component we needed two doublets as well, since the cation environment may be assumed to be independent of the local presence of oxygen vacancies.

The values of IS were characteristic of high spin divalent iron ions in octahedral sites. Assuming similar Debye-Waller factors for the Fe^{3+} and Fe^{2+} components and taking into account their respective spectral area ratios we have estimated the average oxidation state of Fe to be $Fe^{2.6+}$. When comparing the fluorine-free $LiFeO_2$ (LFO) compound with the two fluorinated $Li_{1.25}FeO_2F_{0.25}$ and Li_2FeO_2F compounds (LFF-cs1-25, and LFF-cs2 respectively), one observes remarkably small differences.

The spectra, the hyperfine parameters and the area ratio obtained by an identical fitting strategy, were very similar among the samples. However, a slight increase of the IS of all subspectra upon initial fluorination was observed. This can imply that our reaction pathway followed the Equation (3), forming an F-containing compound. Nevertheless, this trend was not continued in the fully fluorinated sample LFF-cs2, which showed within the error identical values to those of LFF-cs1-25 sample. As Mössbauer is a very sensitive probe of the atom's environment, this behaviour is somewhat surprising. An explanation to this can be the presence of local variations of the atomic species occupancies.

As Richard et al. [2] found out by DFT calculations, the F presence is strongly connected to the formation of the local Li-rich areas, where the amount of the Fe-fluorine bonds is decreased, meaning that with the increase of the F content, the average number of Fe-fluorine bonds stays unchanged.

For the *ms* sample, we have also observed both Fe^{3+} and Fe^{2+} components, however, in this case it is not possible to fit with the 4 components model, and instead 3 components model was used. The distinctly larger linewidth Gamma of the Fe^{2+} component may indicate that either there are only two components, or distribution exists due to the proposed oxygen vacancies.

X-ray absorption spectroscopy has been used as a complementary methodology for the determination of the average Fe valence state in all studied samples. The normalized XANES spectra are plotted in Fig. 5, together with a selected set of XANES spectra of standard reference Fe compounds. Standards were selected based on similar iron coordination

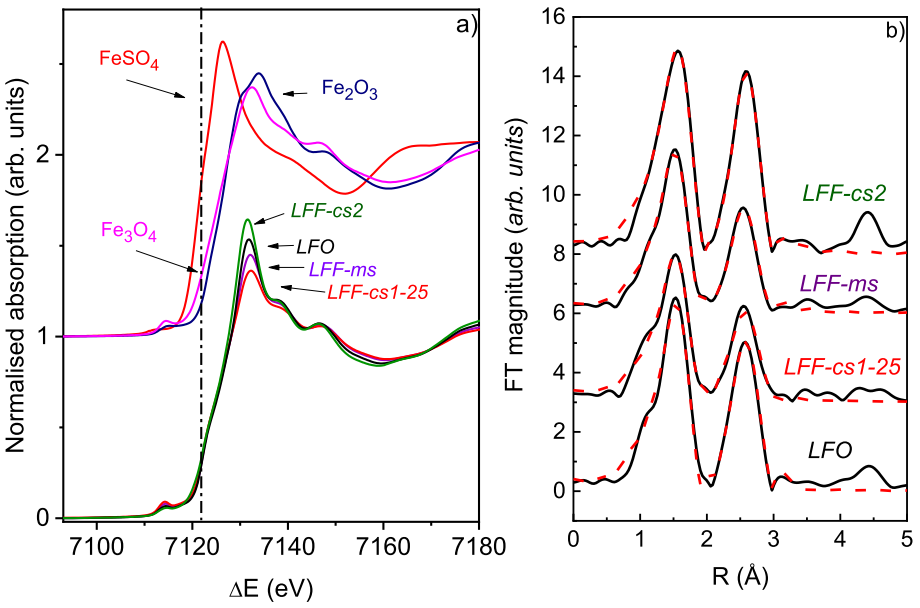

Fig. 4. a) Fe K-edge XANES spectra of lithium iron oxide and oxyfluoride cathode materials with fcc rock-salt structure (LFO, LFF-ms, LFF-cs1-25, LFF-cs2,), and reference iron oxide compounds iron valence states between Fe^{2+} and Fe^{3+} (Fe^{2+}: $FeSO_4 \times 7H_2O$; $Fe^{2.67+}$: Fe_3O_4; Fe^{3+}: Fe_2O_3 (Hematite)). Spectra of reference compounds are shifted vertically for clarity. Vertical dashed line is plotted at the first inflection point of the Fe K-edge (7122 eV) in the reference Fe_3O_4 compound. b) Fourier transform magnitude of k3-weighted Fe EXAFS spectra of lithium iron oxide and oxyfluoride cathode materials with FCC rock-salt structure (LFO, LFF-ms, LFF-cs1-25, LFF-cs2), calculated in the k range of 2.5–13.5 $Å^{-1}$. Experiment – (black solid line); best fit EXAFS model in the R range from 1.0 to 3.4 Å – (red dashed line). (For interpretation of the references to color in this figure legend, the reader is referred to the Web version of this article.)

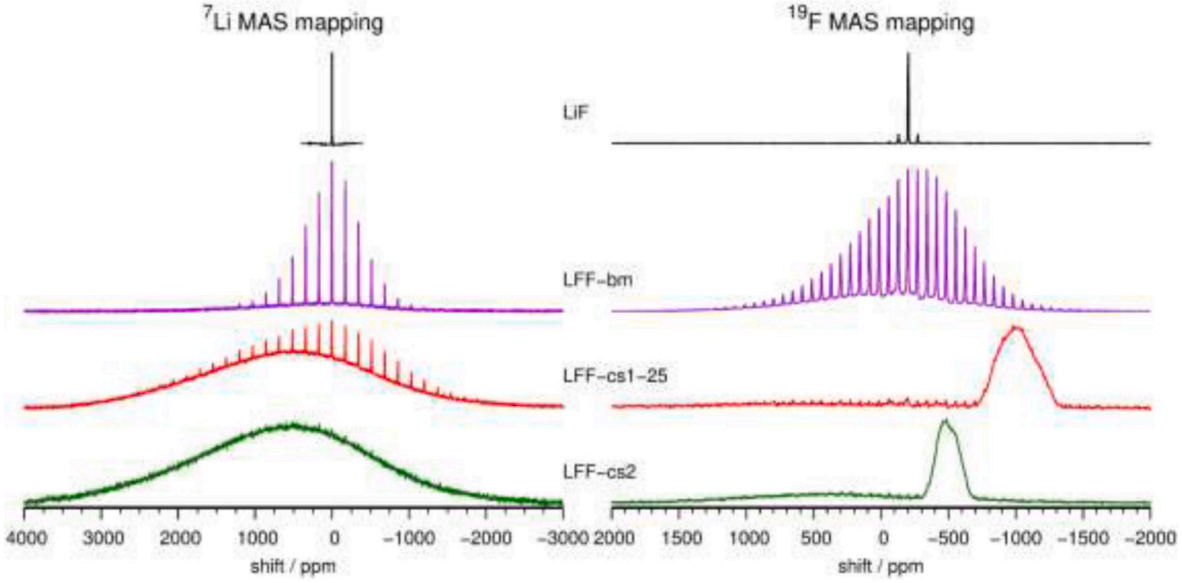

Fig. 5. ^{7}Li and ^{19}F MAS NMR spectra of crystalline LiF and of various LFF samples. As explained in the experimental section, narrow contributions to the ^{19}F MAS NMR spectra are partially suppressed with respect to the broad contributions, meaning that the integrated intensities of the narrow and the broad ^{19}F signals do not accurately reflect the abundancies of fluorine atoms within different environments.

(pure octahedral or mixed octahedral and tetrahedral coordination to oxygen ligands), and different average iron valence states between Fe^{2+} and Fe^{3+} (Fe^{2+} in $FeSO_4 \times 7H_2O$; $Fe^{2.67+}$ in Fe_3O_4 and Fe^{3+} in Fe_2O_3).

The occupancies of the Fe, O and F atoms used as an input for XANES analysis were derived as follows. Li rich oxyfluorides crystallize in *fcc* with NaCl type structure, in which Li and Fe share the same Wyckoff position (*4a*), whereas oxygen and fluorine are sitting in *4b* Wyckoff position [3].

The valence state of Fe cation was deduced from the energy shift of the absorption edge. With increasing oxidation state each absorption feature in the XANES spectrum is shifted to higher energies [19,20]. A shift of the edge position of about 4.5 eV per unit oxidation state between Fe^{2+} and Fe^{3+} is observed on reference compounds (Fig. 4a). If the sample contains cation sites within same compound with different local structure and valence states, then the measured XANES spectrum is a linear combination of individual XANES spectra from different cation sites. Example of such mixed Fe cations compound is crystalline Fe_3O_4 with a cubic inverse spinel structure. Here, one third of Fe cations are in the form of Fe^{2+} and two thirds of the Fe cations are Fe^{3+}. Average valence state of Fe cations in Fe_3O_4 is $Fe^{2.67+}$. The edge position in the XANES spectrum of Fe_3O_4 (Fig. 4a) is between the edge positions of pure Fe^{2+} and Fe^{3+} compounds, with the first inflection point on the rising edge at 7122 eV. Same Fe K-edge energy position is found in all four samples discussed in this work, so we can deduce that average Fe valence state in these materials is between $Fe^{2.6+}$ and $Fe^{2.7+}$. The result is in good agreement with average Fe valence value determined by Mössbauer spectroscopy (Fig. 3 and Table 1).

The shape of the Fe K-edge profile and pre-edge lines in the XANES spectra is sensitive to the changes in the local environment of the Fe cation [21]. In case of XANES spectra of LFO and all the fluorinated

samples (Fig. 4a) we can clearly observe a significant difference between the height of the pre-peak at 7114 eV and resonance above the edge at 7131.5 eV.

The observed differences can be ascribed to small variations in the average Fe local structure in the samples. Details about structural differences in local Fe neighbourhood were obtained from the Fe K-edge EXAFS analysis, which can directly probe the local structure around Fe cations in samples. In Fourier transform magnitude of the Fe K-edge EXAFS spectra (Fig. 4b), which represents average radial distribution of neighbour atoms around Fe cation, two dominant peaks can be seen in the R range between 1 Å and 3.6 Å. They represent the contributions of the photoelectron scattering on the nearest shells of neighbours around the Fe atom. A strong peak in the R range between 1 Å and 2.2 Å can be attributed to photoelectron backscattering on the nearest oxygen neighbours around Fe. The following composed peaks in the R range between 2.5 Å and 3.6 Å represent the contributions from more distant Fe coordination shells in fcc rock-salt structure. For quantitative Fe EXAFS analysis, two FEFF models were constructed.

One was based on the lithium iron oxide ($LiFeO_2$), while the other on was built upon the lithium iron oxyfluoride (Li_2FeO_2F) *fcc* crystal structure. Fe atoms in $LiFeO_2$ crystal structure are surrounded by six oxygen atoms at about 2.0 Å, six Fe and six Li at 3.0 Å, and in third coordination shell eight oxygen neighbours at 3.5 Å (taking into account the occupancy factor of 50% for Li^+ and 50% of Fe^{3+} in the cationic site and the anionic site fully occupied by oxygen [15]). In crystal structure of $Li_{1.25}FeO_2F_{0.25}$, oxygen and fluorine are sitting in *4b* Wyckoff position and Li and Fe share the same Wyckoff position (*4a*). The Fe atoms are octahedraly coordinated to O and F neighbours in first coordination shell, Fe and Li in the second, and O and F in the third coordination shell. The contributions of the first three Fe coordination shells in the R range from 1.0 Å to 3.4 Å (Fig. 4b) were analysed. The FEFF models comprised all single scattering and all significant multiple scattering paths up to 3.6 Å with three variable parameters for each type of neighbour in each coordination shell: coordination shell distance (Δr), and the Debye–Waller (σ2) factors of all single scattering paths and separate Debye–Waller factors of multiple scattering paths. The shell coordination numbers were fixed to the crystallographic values, taking into account the stoichiometric values of the constituent elements in each material. In addition, two common parameters of all scattering paths were also varied in the fits: the amplitude reduction factor S02 and the shift of energy origin of the photoelectron ΔE0.

For all four samples excellent EXAFS fits (Fig. 4b) were obtained in the k range of 2.5–13.5 $Å^{-1}$ and in the R-range of 1.0–3.4 Å. Best fit parameters are listed in the Table SI1 to Table SI4. The results on average local Fe neighbourhood structure for LFO sample agree well with the crystallographic structure data. There are 6 oxygen neighbours at 1.98 Å in first coordination shell, 6 Fe and 6 Li neighbours at slightly different distances around 3.0 Å in the second coordination shell and third coordination shell is composed of 8 oxygen neighbours at 3.56 Å. All Debye-Waller factors are relatively low, indicating small disorder in the structure.

The results on average local Fe neighbourhood structure for LFF-cs2 sample also agree well with the crystallographic structure data of Li_2FeO_2F. In this sample, first coordination shell is composed of 4 oxygen atoms at 1.96 Å and two F atoms at 2.06 Å. In the second coordination shell, there are 4 Fe neighbours at 3.01 Å and 8 Li atoms at 2.80 Å. Finally, the third coordination shell is composed of three fluorine and five oxygen neighbours at 3.41 Å and 3.61 Å, respectively. Also in this structure the Debye-Waller factors are relatively low, indicating small disorder in the structure, except for shell of Li neighbours where the Debye-Waller factor indicates significantly larger disorder. Same result was obtained for LFF-ms sample. Eventual differences in the occupancy of the three neighbour shells could not be reliably detected with EXAFS analysis due to large uncertainties of coordination numbers, if they were also varied in the fit. In case of LFF-cs1-25 sample, the distribution of neighbours in first three coordination shells is the same as described above for LFF-cs2. However, Debye-Waller factors in this sample were significantly larger, indicating significantly larger disorder.

NMR is another spectroscopic technique, being able to detect differences in the local environment of selected elements within solids. In our LFF materials it offers an insight into the environment of Li^+ and F^- ions, and is complementary to Mössbauer and X-ray absorption spectroscopy, which both study the environment of iron. ^{7}Li MAS and ^{19}F MAS NMR spectra of the mechanosynthesized sample and samples obtained by ceramic syntheses are presented in Fig. 5. Most of the ^{7}Li spectra are composed of two contributions, a very broad Gaussian-shaped peak extending between −2000 ppm and 3000 ppm, and a manifold of sharp spinning sidebands (and a center-band) extending between −1500 ppm and 2000 ppm. Relative ratios of these two contributions vary among the samples. In LFF-ms, the signal that is split into a centerband and many spinning sidebands is the dominating contribution. Because the centreband appears close to 0 ppm, this contribution can be assigned to LiF. The fact that the sidebands extend over a very broad frequency range, unlike in pure LiF, where no sidebands can be observed, suggests that LiF is very well mixed or even in close contact with the paramagnetic iron-based phase of this sample. Perhaps this NMR signal does not (only) belong to a separate LiF phase, but (also) to domains rich with Li and F, which are incorporated into the LFO matrix. Indeed, Mössbauer spectroscopy and detailed TEM investigation (below) confirm this hypothesis. The wide manifold of spinning sidebands is much weaker but still clearly detectable in LFF-cs1-25, whereas in LFF-cs2 almost no LiF-like domains can be detected. It should be noted here that the LiF contributions observed by NMR might not always be detectable by XRD. This will especially be the case when they belong to small domains within crystals or to amorphous particles.

The largest fraction of the broad ^{7}Li contribution can be detected in the spectrum of LFF-cs2, suggesting that in this material almost all Li is incorporated within the LFF phase. The reason why this signal is not split into spinning sidebands, in spite of the fast sample spinning at 40 kHz, is because it stems from multiple overlapped signals of different Li environments. As evidenced by Mössbauer and X-ray absorption spectroscopy, Li nuclei within the LFF phase can 'see' various first coordination shells, composed of O^{2-} and F^- anions, and various second coordination shells, composed of Li^+ and paramagnetic $Fe^{3+/2+}$ cations. A similar broad signal was already reported for the lithium manganese oxyfluoride [6].

As ^{7}Li spectra, ^{19}F spectra are also composed of spinning-sideband patterns and of broad, unresolved peaks. The former are the most pronounced in LFF-ms, and can again be assigned to LiF phase or to domains rich in Li and F, strongly affected by proximal paramagnetic iron-based species. The ^{19}F MAS NMR spectra of LFF-cs1-25 and LFF-cs2 are very different from the spectrum of LFF-ms. In addition to weak or negligible sharp sideband patterns, they show prominent broad signal at about −1000 ppm and −500 ppm, respectively. The facts that these two signals are significantly shifted from the position of the diamagnetic LiF signal (resonating at −204 ppm), that they relax very quickly, and that they are not split into spinning sidebands suggest that they could belong to fluorine from the paramagnetic LFF phase (and not from the LiF-like domains within the LFF matrix). The different isotropic shifts and different widths of the two signals are difficult to understand. Perhaps ^{19}F nuclei within LFF-cs1-25 and LFF-cs2 are surrounded by different numbers of iron cations or by iron cations with different oxidation states. Anyhow, the presence of these broad, shifted signals in ^{19}F MAS NMR spectra of LFF-cs1-25 and LFF-cs2 confirms fluorination of the samples obtained by the ceramic synthesis, and shows that following this synthesis route fluorine incorporates into the LFF structure in a completely different manner than the fluorine of the mechanosynthesized sample.

The morphology, distribution of F (Figure SI 6) and atomic structure of LFF-cs2, LFF-ms and LFF-25 samples were investigated by means of TEM. Fig. 6a-c shows the atomic resolution STAM-HAADF images of corresponding samples, with the low magnification images of the

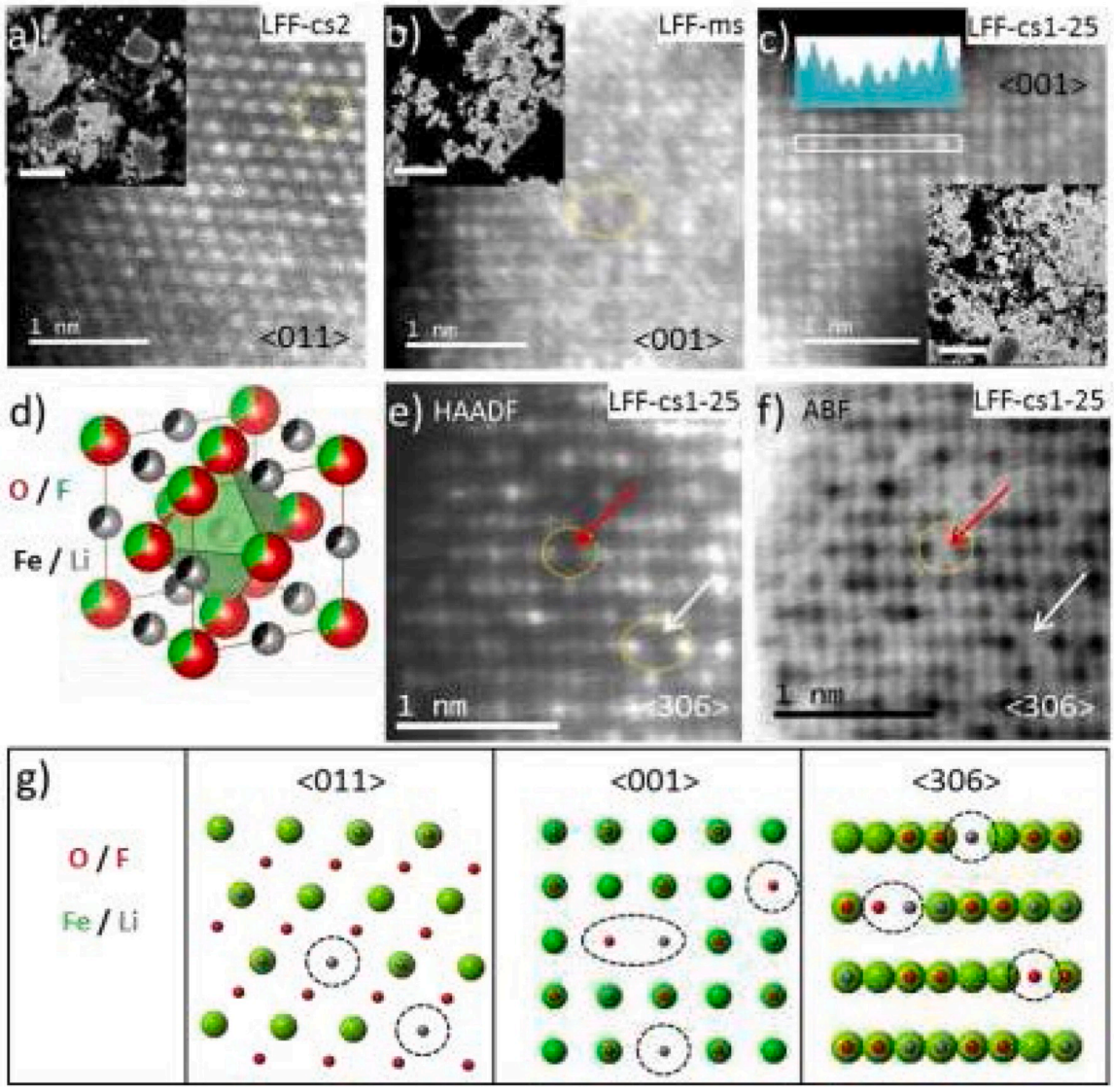

Fig. 6. Atomic resolution STEM-HAADF images of (a) LFF-cs2, (b) LFF-ms and (c) LFF-cs1-25 samples, with the low magnification shown on the insets; (d) atomic structure of LFF; (e) STEM-HAADF and (f) STEM-ABF images of LFF-cs1-25 sample taken in <306> zone axis, showing cation disorder, which are sketched in (g). The scale bar of the insert is 2 μm.

powder particle size distribution in the insets. Here, the LFF-cs1-25 sample revealed the smallest particles with rather small grain sizes distribution. Both LFF-cs1-25 and LFF-cs2 samples possess the highest crystallinity, and LFF-ms sample shows the most disturbed atomic columns arrangement. In all 3 samples one can notice the intensity variation of the atomic columns. Such variations in STEM-HAADF images arise from the variations in the atomic number of the species occupying positions in the LFF lattice and imply the solid solution-type distribution of Li, Fe, F and O atoms. The example intensity profile over the selected atomic columns row is shown on the inset in Fig. 6c for the LFF-cs1-25 sample. The observed intensity variations are due to the larger number of Fe atoms occupying the Fe/Li site in the particular atomic column in the viewing direction. This solid solution-type atomic species site occupancy was observed in all three investigated samples (Fig. 6d–g). It also can be noticed, that these intensity variations are not a single type events. Instead, they are grouped together (Fig. 6e–f), forming 3D nano-domains of specific species distribution throughout the whole lattice structure. While the dark areas marked by the red and white arrows in Fig. 6e STEM-HAADF image appear similarly empty, STEM-ABF imaging allows us to see whether the site is actually vacant (marked by the red arrow), or it is occupied by the Li atomic column (marked by the white arrow). The presence of such arranged nano-domains of atomic species goes in accordance with the better electrochemical performance of the samples with higher crystallinity, such as LFF-cs1-25.

Electrochemical characterization: The lithium-ion insertion/extraction reaction from $Li_{1+x}FeO_2F_x$, (with $x = 0, 0.25, 1$) relies on the reversibility of the Fe^{3+}/Fe^{2+} redox couple. The electrochemical reaction associated can be summarized in the Equation (5) as:

$$Li_{1+x}Fe^{III}O_2F_x + Li^+ + e^- \rightarrow Li_{2+x}Fe^{II}O_2F_x \quad (5)$$

With a given theoretical capacities of 283 mA h/g; 265 mA h/g; and 222 mA h/g for $LiFeO_2$; $Li_{1.25}FeO_2F_{0.25}$ and Li_2FeO_2F respectively. In this study, all the samples were cycled starting by the reduction (discharge) followed by a subsequent oxidation (charge) of the cathode materials (Fig. 7a–d). The sloping curve indicates that incorporation of Li^+ is a solid solution mechanism (see the GITT measurements in Figure SI7). Regarding $LiFeO_2$ the solid solution mechanism was well demonstrate by several authors [18,21–23]. Compared samples are showing a distinct differences in the capacity which can be correlated to differences in the occupation and doping leading to different level of

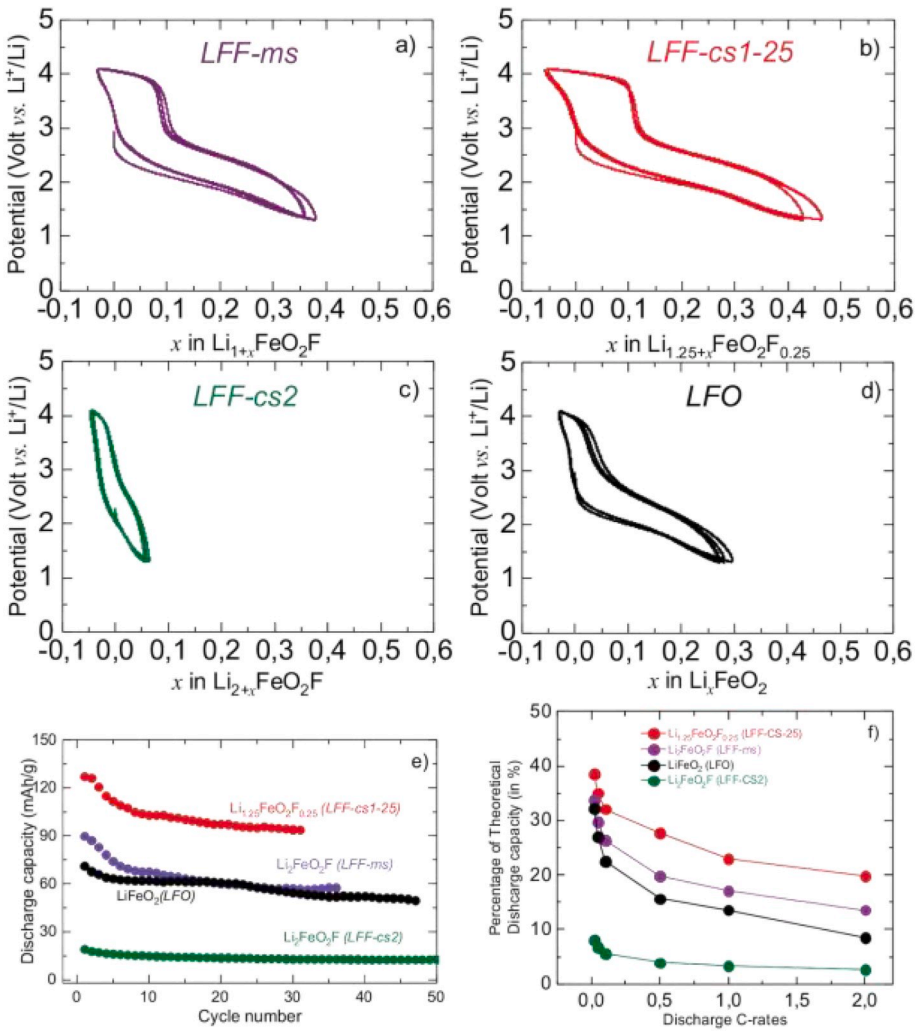

Fig. 7. Electrochemical behaviour of different Fe based lithium rich materials. Galvanostatic cycling at C/20 (a-e) and C-rate performance (f). Electrodes were cycled between 3.00 and 1.30 V vs. Li+/Li.

disorder.

Two samples obtained by ceramic synthesis, LFF-cs1-25 (Fig. 7b) and LFF-cs2 (Fig. 7c) exhibit completely different electrochemical properties. Partially doping leads to high electrochemical activity, even higher compared sample obtained by mechanochemical synthesis. As suggested by Richard et al. [2] by DFT calculations and confirmed in this study by Mössbauer, XAS and TEM, the F presence is strongly connected to the formation of the local Li-rich areas, where the amount of the Fe-fluorine bonds is decreased. Simultaneously, some local Fe-rich areas are present in which the extra Li^+ can be stored, and Fe been reduced. Inhomogeneous distribution of cations have beneficial impact on the specific capacity and can be obtained by controlled synthesis with low level of doping.

Electrochemical stability has been checked by continuous cycling and we didn't observe any severe degradation during the initial cycling (Fig. 7e). Samples were tested at different C-rates to check their capability at higher current densities. Fig. 7f shows measured capacities expressed as percentage of theoretical capacity for C-rates between C/20 and 2C. In line with the above discussion, partially doped sample (LFF-cs1-25) exhibit the best kinetical properties due to the lowest capacity drop with increased current density. Preliminary work by electrochemical impedance spectroscopy (EIS) shows that at the OCV, the EIS at low frequency is dominated by Warburg diffusion. At the end of discharge, the EIS at low frequency is almost parallel to the imaginary axis. This is characteristic of a blocking electrode. The process is reversible since during subsequent charge, the EIS at low frequencies again becomes inclined at 45°.

We extended the ceramic synthesis study to the lithium titanium oxyfluorides. Synthesis at temperature higher than 900 °C leads to the formation of the spinel $LiTiO_2$. Figure SI8 shows the XRD pattern of titanium based materials obtained after the optimisation of cs1 (LTF-cs1-25) and cs2 (LTF-cs2). One can observed the increase of the lattice parameters with the higher amount of LiF in the structure. Galvanostatic curves and cycling stability are shown in the Fig. 8. Similarly as already observed for Fe based materials, TEM images of LTF-cs1-25 and LTF-ms exhibits 2 different heterogeneous domains: the region rich in transition metal (here Ti) and the area rich in Li. Those domains are agglomerated for both LTF-cs1-25 and LTF-ms. We can correlate the higher capacity to the presence of higher rich Li domains.

4. Conclusions

Ceramic synthesis routes were developed for the synthesis of lithium rich iron(titanium) oxyfluorides with different level of doping. Two different synthesis procedures lead to materials with maximum doping of x = 0.25 and x = 1 in $Li_{1+x}MO_2F_x$ composition. Level of doping depends on the selected precursors. Samples with iron as transition metals were truly characterised by means of several complementary analytical techniques. The XAS showed that the average oxidation state of iron in both materials is between $Fe^{2.6+}$ and $Fe^{2.7+}$. This value was further

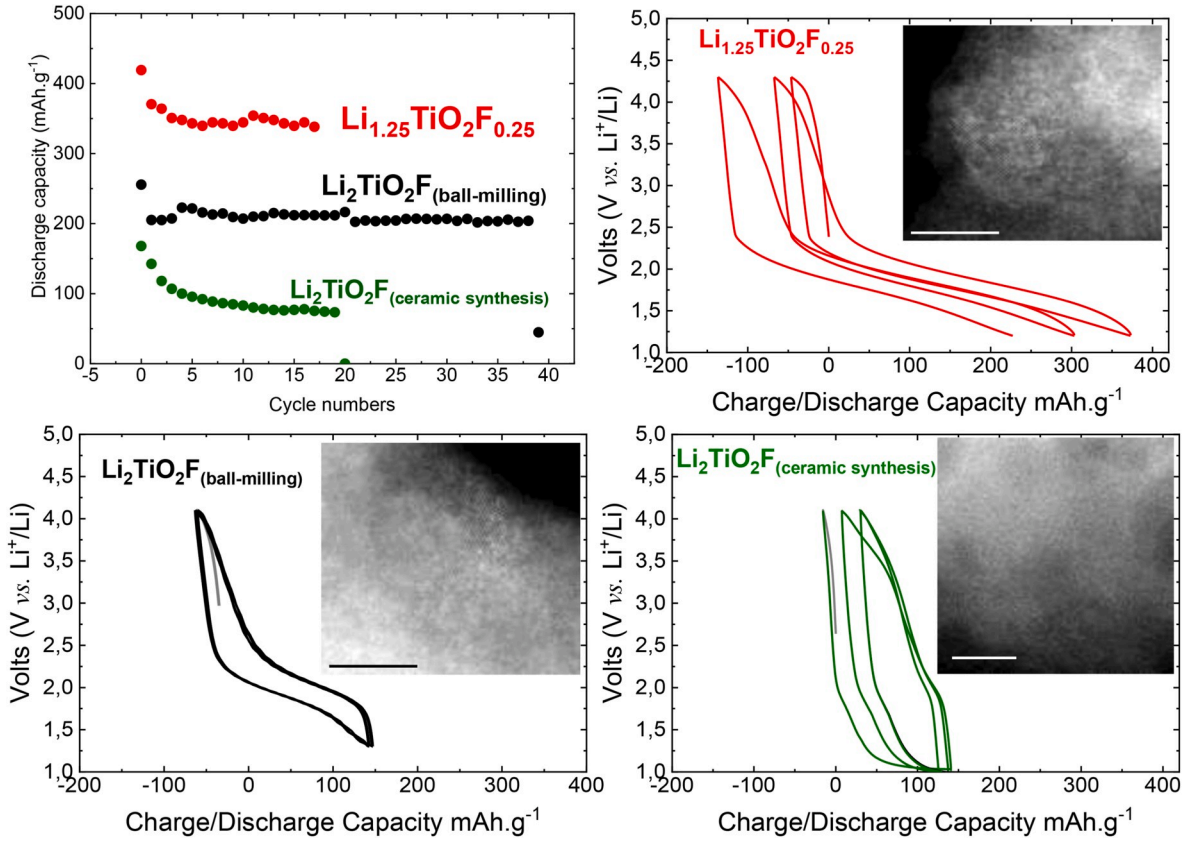

Fig. 8. Electrochemical behaviour of different Ti based lithium rich materials. Characteristic TEM images are inserted for each material (scale bar corresponds to 5 nm). Electrodes were cycled between 4.10 and 1.30 V vs. Li^+/Li at C/20.

confirmed by Mössbauer for which presence of Fe^{2+} was spotted explaining the reduced average oxidation state of iron. Moreover, EXAFS revealed a more disorder structure for $Li_{1.25}FeO_2F_{0.25}$ (LFF-cs1-25) than for Li_2FeO_2F (LFF-cs2). That disorder was further observed by TEM for which it was evidenced that larger numbers of iron atoms are occupying the Fe/Li site. More defects were observed for $Li_{1.25}FeO_2F_{0.25}$ than for Li_2FeO_2F. Interestingly, those defects were clustered and segregated in two domains: rich in Li and rich in Fe. This was further confirmed by Li NMR. Indeed extended sidebands over a very broad frequency range in the case of $Li_{1.25}FeO_2F_{0.25}$, suggests that there is more Li-rich domain (observed in TEM) in $Li_{1.25}FeO_2F_{0.25}$ than for Li_2FeO_2F. Those clustered Li-rich domains highlight the presence of more defects in $Li_{1.25}FeO_2F_{0.25}$. Observed diversity in the cation distribution between two samples lead to different electrochemical activity of two samples. Electrochemical activity of $Li_{1.25}FeO_2F_{0.25}$ (LFF-cs1-25) sample is much higher compared to the electrochemical activity of fully doped Li_2FeO_2F due to much easier lithium diffusion through lithium rich domains in the material. That was further confirmed with titanium based lithium rich oxyfluoride samples, where again much higher electrochemical activity has been obtained with sample $Li_{1.25}TiO_2F_{0.25}$ in comparison with Li_2TiO_2F. Similar as in $Li_{1.25}FeO_2F_{0.25}$ (LFF-cs1-25) sample we observed lithium rich domains within the sample LTF-cs1-25 ($Li_{1.25}TiO_2F_{0.25}$). Results in this work show the necessity for optimisation of level of doping in order to facilitate lithium transport within rock salt structure and to keep high electrochemical activity by obtaining full electrochemical capacity.

Associated content

Supporting Information contains schematic of the reactor used for the synthesis and additional crystallographic information about materials, EIS spectra and tables containing Neutron diffraction refined values. All that is available from the Wiley Online Library or from the author.

Declaration of competing interest

The authors declare that they have no known competing financial interests or personal relationships that could have appeared to influence the work reported in this paper.

CRediT authorship contribution statement

Jean-Marcel Ateba Mba: Conceptualization, Methodology, Writing - original draft. **Iztok Arčon:** Data curation, Formal analysis. **Gregor Mali:** Data curation, Formal analysis. **Elena Tchernychova:** Data curation, Formal analysis. **Ralf Witte:** Formal analysis. **Robert Kruk:** Data curation. **Miran Gaberšček:** Formal analysis. **Robert Dominko:** Conceptualization, Supervision, Writing - review & editing.

Acknowledgment

We acknowledge access to the SR facilities of ELETTRA (beamline XAFS, pr. 20175158). We would like to thank Simone Pollastri, Mateusz Czyzycki, Giuliana Aquilanti, and Luca Olivi of ELETTRA for assistance during the experiment. We acknowledge Sorour Semsari Parapari for technical support and Andy Naylor from Uppsala University for Neutron spectra measurements. This research was supported by the project LiRichFCC under the Grant Agreement No 711792 from the EU Horizon 2020 research and innovation programme, by the Slovenian Research Agency (core research programs P1-0112 and P2-0393), and by the project CALIPSOplus under the Grant Agreement 730872 from the EU Framework Programme for Research and Innovation HORIZON 2020.

Appendix A. Supplementary data

Supplementary data to this article can be found online at https://doi.org/10.1016/j.jpowsour.2020.228230.

References

[1] M. Obrovac, Structure and electrochemistry of $LiMO_2$ (M=Ti, Mn, Fe, Co, Ni) prepared by mechanochemical synthesis, Solid State Ionics 112 (1–2) (1998) 9–19, https://doi.org/10.1016/S0167-2738(98)00225-2.

[2] W.D. Richards, S.T. Dacek, D.A. Kitchaev, G. Ceder, Fluorination of lithium-excess transition metal oxide cathode materials, Adv. Energy Mater. (2017), https://doi.org/10.1002/aenm.201701533.

[3] R. Chen, S. Ren, M. Knapp, D. Wang, R. Witter, M. Fichtner, H. Hahn, Disordered lithium-rich oxyfluoride as a stable host for enhanced Li^+ intercalation storage, Adv. Energy Mater. 5 (9) (2015), https://doi.org/10.1002/aenm.201401814.

[4] R. Chen, S. Ren, M. Yavuz, A.A. Guda, V. Shapovalov, R. Witter, M. Fichtner, H. Hahn, Li^+ intercalation in isostructural Li_2VO_3 and Li_2VO_2F with O^{2-} and mixed O^{2-}/F^- anions, Phys. Chem. Chem. Phys. 17 (26) (2015) 17288–17295, https://doi.org/10.1039/C5CP02505B.

[5] R. Chen, S. Ren, X. Mu, E. Maawad, S. Zander, R. Hempelmann, H. Hahn, High-performance low-temperature Li+ intercalation in disordered rock-salt Li–Cr–V oxyfluorides, ChemElectroChem 3 (6) (2016) 892–895, https://doi.org/10.1002/celc.201600033.

[6] R.A. House, L. Jin, U. Maitra, K. Tsuruta, J.W. Somerville, D.P. Förstermann, F. Massel, L. Duda, M.R. Roberts, P.G. Bruce, Lithium manganese oxyfluoride as a new cathode material exhibiting oxygen redox, Energy Environ. Sci. 11 (4) (2018) 926–932, https://doi.org/10.1039/c7ee03195e.

[7] A. Urban, J. Lee, G. Ceder, The configurational space of rocksalt-type oxides for high-capacity lithium battery electrodes, Adv. Energy Mater. 4 (13) (2014) 1–9, https://doi.org/10.1002/aenm.201400478.

[8] J. Lee, D.A. Kitchaev, D. Kwon, C. Lee, J.K. Papp, Y. Liu, Z. Lun, Lithium-Excess Cathode Materials, 2018, https://doi.org/10.1038/s41586-018-0015-4.

[9] C. Baur, J. Chable, F. Klein, V.S.K. Chakravadhanula, M. Fichtner, Reversible delithiation of disordered rock salt LiVO2, ChemElectroChem 5 (11) (2018) 1484–1490, https://doi.org/10.1002/celc.201800189.

[10] G. Aquilanti, M. Giorgetti, R. Dominko, L. Stievano, I. Arčon, N. Novello, L. Olivi, Operando characterization of batteries using X-ray absorption spectroscopy: advances at the beamline XAFS at synchrotron Elettra, J. Phys. D Appl. Phys. 50 (7) (2017), https://doi.org/10.1088/1361-6463/aa519a.

[11] B. Ravel, M. Athena Newville, Hephaestus Artemis, Data analysis for X-ray absorption spectroscopy using IFEFFIT, J. Synchrotron Radiat. (2005).

[12] J.J. Rehr, R.C. Albers, S.I. Zabinsky, High-order multiple-scattering calculations of x-ray-absorption fine structure, Phys. Rev. Lett. 69 (23) (1992) 3397–3400, https://doi.org/10.1103/PhysRevLett.69.3397.

[13] A.J. Pell, R.J. Clement, C.P. Grey, L. Emsley, G. Pintacuda, Frequency-stepped acquisition in nuclear magnetic resonance spectroscopy under magic angle spinning, J. Chem. Phys. 138 (11) (2013) 114201, https://doi.org/10.1063/1.4795001.

[14] A. Du Pasquier, P.C. Warren, D. Culver, A.S. Gozdz, G.G. Amatucci, J.M. Tarascon, Plastic PVDF-HFP electrolyte laminates prepared by a phase-inversion process, Solid State Ionics 135 (1–4) (2000) 249–257, https://doi.org/10.1016/S0167-2738(00)00371-4.

[15] D.E. Cox, G. Shirane, P.A. Flinn, S.L. Ruby, W.J. Takei, Neutron diffraction and mössbauer study of ordered and disordered LiFeO2, Phys. Rev. 132 (4) (1963) 1547–1553, https://doi.org/10.1103/PhysRev.132.1547.

[16] O. Knop, C. Ayasse, J.S. Carlow, W.W. Barkers, F.W.D. Woodhams, R.E. Meads, W. G. Parker, Origin of the quadrupole splitting of cubic (disordered) in the miissbauer 67Fe spectrum, 1978, pp. 329–346.

[17] M.C. Blesa, E. Moran, C. Leon, J. Santamaria, J.D. Tornero, N.A. Menendez, NaFeO 2 : Ionic conductivity and sodium extraction 126 (1999) 81–87.

[18] M. Hirayama, H. Tomita, K. Kubota, R. Kanno, Structure and electrode reactions of layered rocksalt LiFeO 2 nanoparticles for lithium battery cathode, J. Power Sources 196 (16) (2011) 6809–6814, https://doi.org/10.1016/j.jpowsour.2010.10.009.

[19] I. Arčon, J. Kolar, D. Hanžel, M. Strlič, XANES analysis of Fe valence in iron gall inks, X Ray Spectrom. 36 (2007) 199–205, https://doi.org/10.1002/xrs.

[20] R. Dominko, C. Sirisopanaporn, C. Masquelier, D. Hanzel, I. Arcon, M. Gaberscek, On the origin of the electrochemical capacity of Li[sub 2]Fe[sub 0.8]Mn[sub 0.2]SiO[sub 4], J. Electrochem. Soc. 157 (12) (2010) A1309, https://doi.org/10.1149/1.3491368.

[21] Y. Sakurai, Preparation of electrochemically active α-LiFeO2 at low temperature, Solid State Ionics 113–115 (1–2) (1998) 29–34, https://doi.org/10.1016/S0167-2738(98)00363-4.

[22] Y. Sakurai, H. Arai, S. Okada, J.I. Yamaki, Low temperature synthesis and electrochemical characteristics of LiFeO2cathodes, J. Power Sources 68 (2) (1997) 711–715, https://doi.org/10.1016/S0378-7753(96)02579-7.

[23] S. Wu, H. Liu, Preparation of LiFeO2-based cathode materials by an ionic exchange method, 174, 2007, pp. 789–794, https://doi.org/10.1016/j.jpowsour.2007.06.230.